PAPER

Helical neural implants for intracerebral drug delivery

Journal of Neural Engineering

RECEIVED
14 July 2025

ACCEPTED FOR PUBLICATION
8 September 2025

PUBLISHED
29 September 2025

PAPER

Helical neural implants for intracerebral drug delivery

Batoul Khlaifat[1,2,6], Mahmoud Elbeh[1,3,6], Shreya Manjrekar[1], Seung-Jean Kang[1], Yusheng Zhang[1,3], Parima Phowarasoontorn[1,2,4], Sadaf Usmani[1], Abdel-Hameed Dabbour[1,4], Heba T Naser[1,4], Hanan Mohammed[1,4], Minsoo Kim[1] and Khalil B Ramadi[1,2,3,4,5,*]

[1] Division of Engineering, New York University Abu Dhabi, Abu Dhabi, United Arab Emirates
[2] Center for Brain and Health, New York University Abu Dhabi, Abu Dhabi, United Arab Emirates
[3] Tandon School of Engineering, New York University, New York, NY 11201, United States of America
[4] Center for Translational Medical Devices, New York University Abu Dhabi, Abu Dhabi, United Arab Emirates
[5] Grossman School of Medicine and NYU Langone Health, New York University, New York, NY 11201, United States of America
[6] These authors contributed equally to this work.
[*] Author to whom any correspondence should be addressed.

E-mail: kramadi@nyu.edu

Keywords: microfluidics, drug delivery, intracerebral infusion, implantable devices, helical catheter

Supplementary material for this article is available online

Abstract

Objective. Neurological disorders often arise from specific regions of dysfunction in the brain. One approach to target these pathologic regions is through chemical delivery using intracerebral implants. Previous works have designed implants that are small and flexible, minimizing the mechanical mismatch between inorganic implants and soft organic brain tissue. Most of these implants are simple cylindrical catheters with inflow and outflow ports at either end of the cylinder. This limits the region and volume of tissue that can be dosed. We sought to develop novel catheter designs that permit targeting of larger volumes of brain tissue while maintaining minimal footprint to minimize gliosis. *Approach.* We present the design, fabrication, and testing of a novel helical-shaped microfluidic catheter we term SPIRAL (Strategic Precision Infusion for Regional Administration of Liquid). SPIRAL leverages rational fluidic design of multiple fluid outflow ports to vary infused fluid spatial distribution across brain regions. We used *in silico, in vitro, and in vivo* models to test the fluid dynamic functionality and chronic viability of SPIRAL. *Results.* Our computational fluid dynamics (CFDs) models illustrate how SPIRAL can be configured to permit simultaneous dosing through multiple outflow ports yielding a variable fluid distribution compared to a straight catheter. We show how CFD *in silico* models can be used to optimize dimensions of channel openings across SPIRAL, to achieve uniform flow through channels and validate these results *in vitro*. We show how chronically implanted SPIRAL catheters do not increase gliosis compared to standard straight catheters of similar dimensions or materials. *Significance.* Our helical intracerebral drug delivery catheter facilitates fluid localization while maintaining minimal invasiveness. SPIRAL could enable multiregional brain access and improve therapeutic efforts in the treatment of neurological diseases.

1. Introduction

Neurological disorders including Parkinson's, epilepsy, and brain tumors account for a significant percentage of deaths worldwide [1]. Despite advancements in medical research and novel therapies such as monoclonal antibodies and gene therapy, treatment of brain conditions faces several challenges, a significant one being the blood brain barrier (BBB). The BBB is a highly selective semi permeable barrier that protects the brain from pathogens and harmful substances [2]. However, this also severely restricts the passage of therapeutic compounds [2]. In addition, systemically administered drugs often yield adverse side effects, which can limit dosages to suboptimal therapeutic levels [3]. Nanoformulation of

drugs can increase selective uptake in the brain, however nanocarrier therapy can hinder drug efficacy and accentuate tissue toxicity [3–5].

One potential way to target pathologic regions in neurologic diseases is through localized drug delivery where catheters can be implanted, targeting the region of interest. Catheters often utilize single-lumen, rigid cylindrical shapes implanted chronically or temporarily to dose a brain target. Therapies can then be infused through Ommaya reservoirs or implanted pumps [6]. Once infused, the distribution of drug is then governed by diffusion or convection, depending on the approach taken to infuse the drug. Diffusive distribution relies on low infusion velocities, and thus is largely limited to small volumes, making it impractical for delivering therapeutic concentrations across larger brain regions. Convection-enhanced delivery (CED) utilizes high pressure and injection velocity to drive convection through a broader region [6–8]. However, the success of CED in dosing larger volumes of brain is often challenged by the backflow of infusate. Backflow is more pronounced with greater infusion velocities and occurs due to a combination of pressure-driven tissue-implant separation and mechanical disruption [9]. Efforts to mitigate backflow in CED have included the use of step-design catheters, micro-porous catheters, and optimized infusion rate protocols [10–12]. While some of these approaches have shown marginal improvements in specific contexts, none have fully addressed the fundamental challenge of achieving consistent, widespread, and controllable distribution, particularly in heterogeneous brain tissue or for non-spherical targets. Targeting irregularly-shaped regions not spherically circumscribed requires multiple boluses often delivered sequentially via repeated catheter insertions, or simultaneously with multiple co-implanted catheters which significantly increases trauma to the brain and resulting gliosis [13].

We posited that multiple boluses could be delivered by utilizing catheters with multiple outflow ports along its length. We further hypothesized that the overall dosed region could be varied by updating the catheter shape from a single cylinder to a helix (figures 1(A)–(E)). Previous work has shown that the primary driver of gliosis around brain implants is their diameter [14]. We therefore reasoned that a restructuring of a straight cylindrical catheter into a helical shape of similar diameter will not increase neuroinflammatory response in the brain. We illustrate that (1) designing catheters with multiple outflow ports and using rational fluidic design can determine flow rate through each port *a priori*, and (2) reshaping of a cylindrical catheter into a helical shape can span a larger area of brain while maintaining a similar footprint as a cylindrical catheter equivalent (figure 1).

Table 1. Diameter, viscosity, and velocity values used across scale models to maintain dynamic similarity.

Scale	1x	25x	4x
Diameter (mm)	0.2	5	0.8
Kinematic viscosity ($m^2\ s^{-1}$)	1×10^{-6}	1.33×10^{-3}	1×10^{-6}
Velocity ($m\ s^{-1}$)	8.84×10^{-5}	4.69×10^{-3}	2.21×10^{-5}

2. Results

Adding multiple outflow ports along a single straight catheter can theoretically permit a variety of dosing geometries (figures 1(A)–(C)). A helical structure entails a major diameter that occupies space in the *X* and *Y* axes allowing for a broader distribution along its dimensions. Changing catheter shape into a helix further adds variability in the ability to dose complex regions simultaneously (figures 1(D) and (E)). This can be done by varying the helix major diameter, maintaining the same catheter diameter.

We first sought to understand how placing multiple outflow ports along the length of a cylindrical catheter could influence rates through each. We conducted a computational fluid dynamics (CFDs) simulation of laminar flow through a straight catheter with four outlets of identical diameter along the cylinder length. We modeled a catheter length of 16 mm, diameter 0.3 mm (inner inlet diameter: 0.2 mm), reasoning that such dimensions are regularly implanted in rats for infusion studies [15]. We arrived at specific distribution of the outlet sizes in figures 2(A) and (B) that equalize outflow through each outlet. We used a 10 $\mu l\ hr^{-1}$ infusion rate and found that this configuration results in 2.38 $nl\ s^{-1}$ flow delivered through the first outlet (figure 2(C)). The fourth and largest outlet pair holds the same value at 100 μm throughout the iterative process, while we tweaked the diameter of the first three outlets from the original starting point window (figure 2(D)). We iterated algorithmically until the flow rate through all outlets were equal, and discovered that small variations in outflow port sizes had large effects on fluid distribution (figures 2(C)–(E)). Outlet diameter of 39.54, 47, 61.2, 100 μm ensured a final equal flow rate of 0.69 $nl\ s^{-1}$ (figure 2(E)).

We next applied this approach to a helical catheter model of identical diameter and length, starting with the final outlet sizes derived for the straight catheter (figures 2(F)–(G)). Changing the catheter geometry induced an average of 14.63% change in outlet flow distribution (figure 2(H)). Our algorithm converged to outlets with diameter of 37.4, 44.6, 58.2, 100 μm to achieve equal flow rate across all outlets (figure 2(J)). Figures 2(B) and (G) show the final outlets' diameters

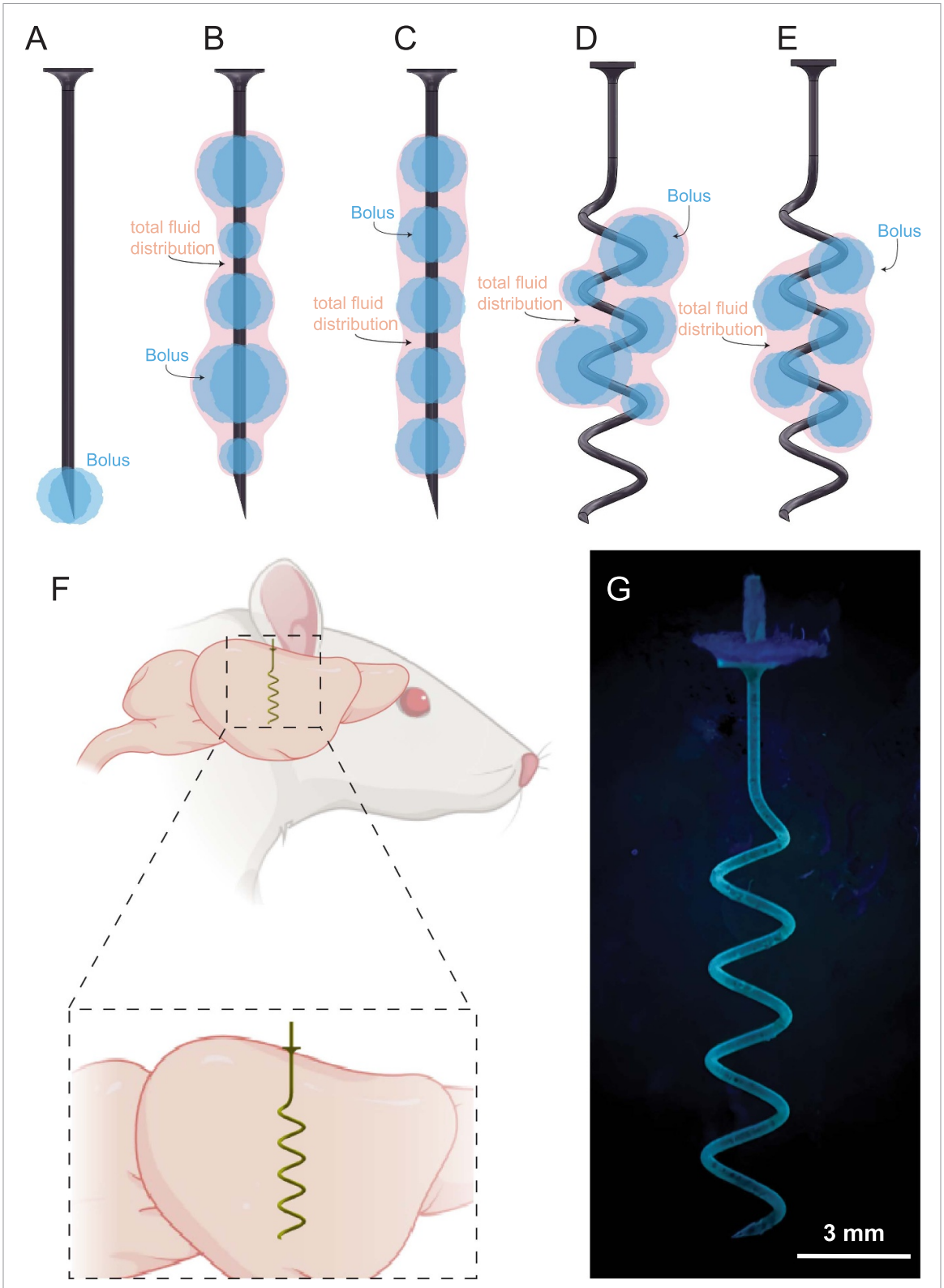

Figure 1. (A) straight catheter with the fluid bolus out of one outlet (B) straight catheter with the fluid bolus out of five pairs of outlets, unequal total fluid distribution (C) straight catheter with equal total fluid distribution out of five pairs of outlets (D) helical catheter with unequal total fluid distribution out of five pairs of outlets (E) helical catheter with equal total fluid distribution out of five pairs of outlets (F) illustration of the helical device in the brain (G) 3D printed helical device imaged under UV light.

annotated relative to the fourth and largest diameter for both the straight and helical models.

We then experimentally validated the computational model using a scaled-up version (25X) of the cylindrical catheter with a new inner inlet diameter of 5 mm. We calculated the equivalent flow rate and viscosity required to replicate the conditions set forth in the simulation while maintaining the Reynold's number ascribed from the computational simulation, to maintain dynamic similarity and flow regime

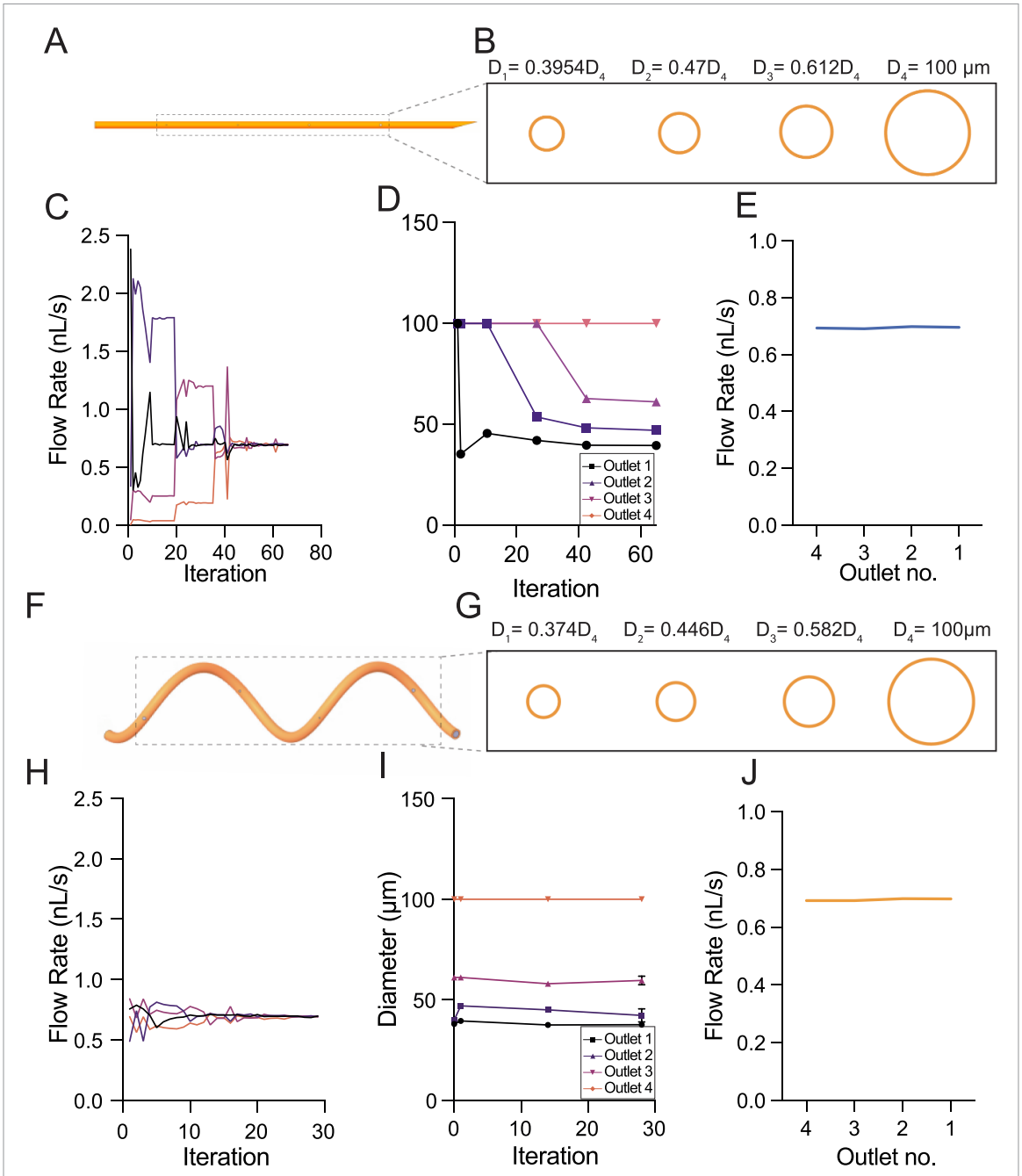

Figure 2. (A) Schematic of straight catheter (B) computationally derived outlet diameters that equalize flow across 4 different outlets in the straight catheter (C) algorithmic changes applied to converge the volumetric fluid flow (D) algorithmic changes applied to the straight catheter's four outlets' diameters (E) volumetric flow rate (nl s^{-1}) of the four outlet pairs of the linear catheter (F) schematic of the helical catheter (G) computationally derived outlet diameters that equalize flow across 4 different outlets in the helical catheter (H) algorithmic changes applied to converge the volumetric fluid flow (I) algorithmic changes applied to the helical catheter's four outlets' diameters (F) volumetric flow rate (nl s^{-1}) of the four outlet pairs of the helical catheter.

(table 1). Reynold's number (Re) is a dimensionless parameter used to characterize flow, and is defined as:

$$\mathrm{Re} = \frac{\rho V D}{\mu} = \frac{V D}{\nu}$$

(where ρ is the fluid density, V is the fluid velocity, D is the diameter of catheter, μ is the dynamic viscosity, ν is kinematic viscosity)

We estimated a Reynold's number of 0.0176 in the simulation, based on flow rate of 10 μl hr^{-1} and assuming water with dynamic viscosity 1 mPa s. We maintained Reynold's number in our scaled up experimental set up using a mixture of corn syrup and water with a final density of 1317 kg m^{-3}, and dynamic viscosity of 1.75 Pa · s. Average velocity was then calculated to be 4.69×10^{-3} m s^{-1}, equivalent to a flow rate to be 5.5 ml min^{-1}.

We used two vertically, but angularly opposite mirrors to project infusate droplets out the outflow ports as they settle on the platform during infusion (figures 3(A)–(C)). By measuring the droplet

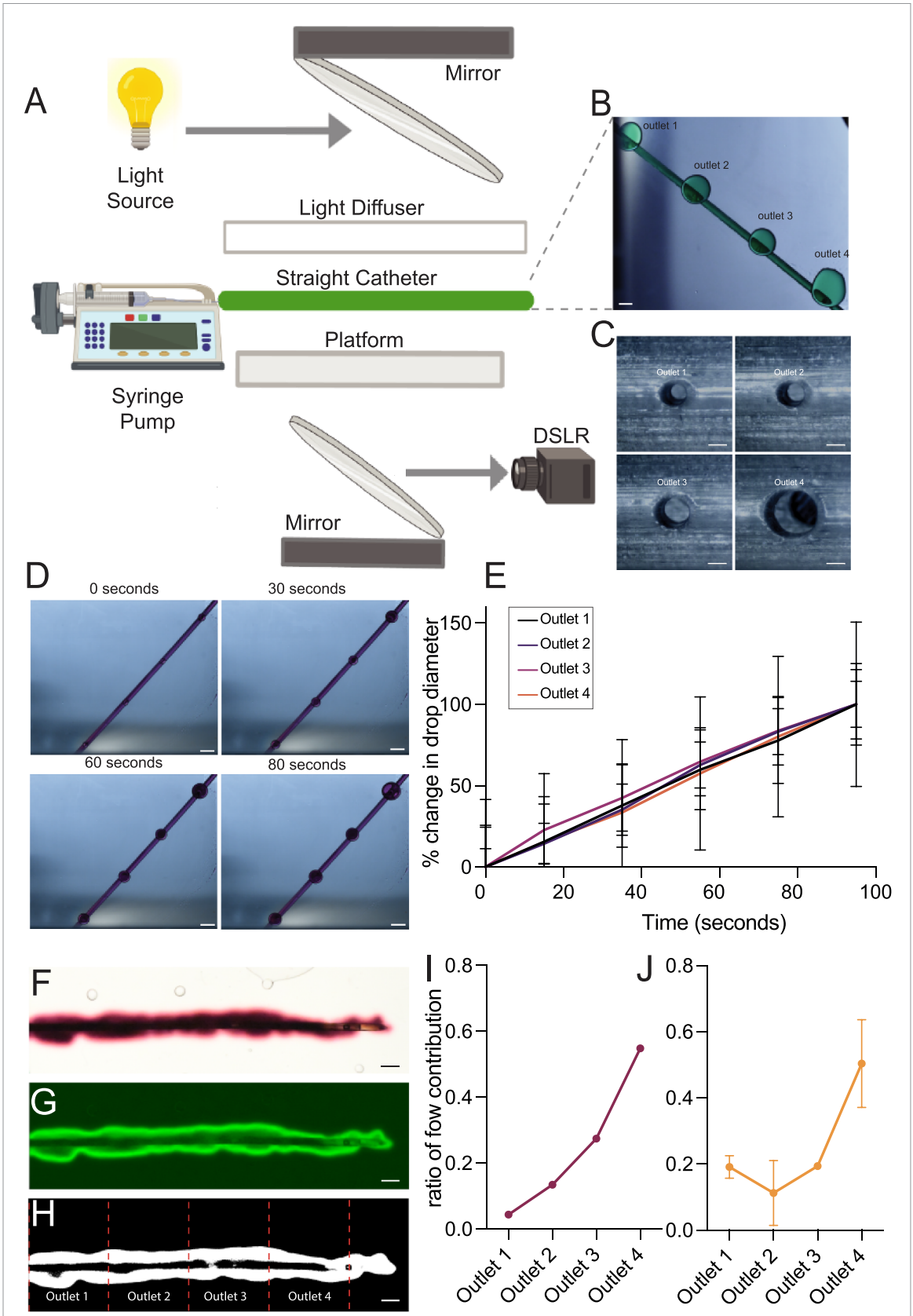

Figure 3. (A) Side view schematic of the fluid flow test set up, (B) fluid flow image of the 25X model taken through set up at SITES lab (NYUAD) scale bar: 20 mm, (C) stereo microscope images of outlets 1 through 4 of 25X model. Scale bar: 1 mm (D) time- dependent images of the droplets. Scale bar: 20 mm (E) comparative drop size analysis of the fluid flow through the different outlets of the 25X model. (F) Image of dye diffusion out of a 4X model in brain phantom scale bar: 3 mm (G) L(A)B stack image of the model processed on ImageJ (H) binary processed image with diffusion out of the four outlets. (I) Ratio of flow contribution of the simulated outlets (J) ratio of flow contribution of the outlets of 4X model in brain phantom.

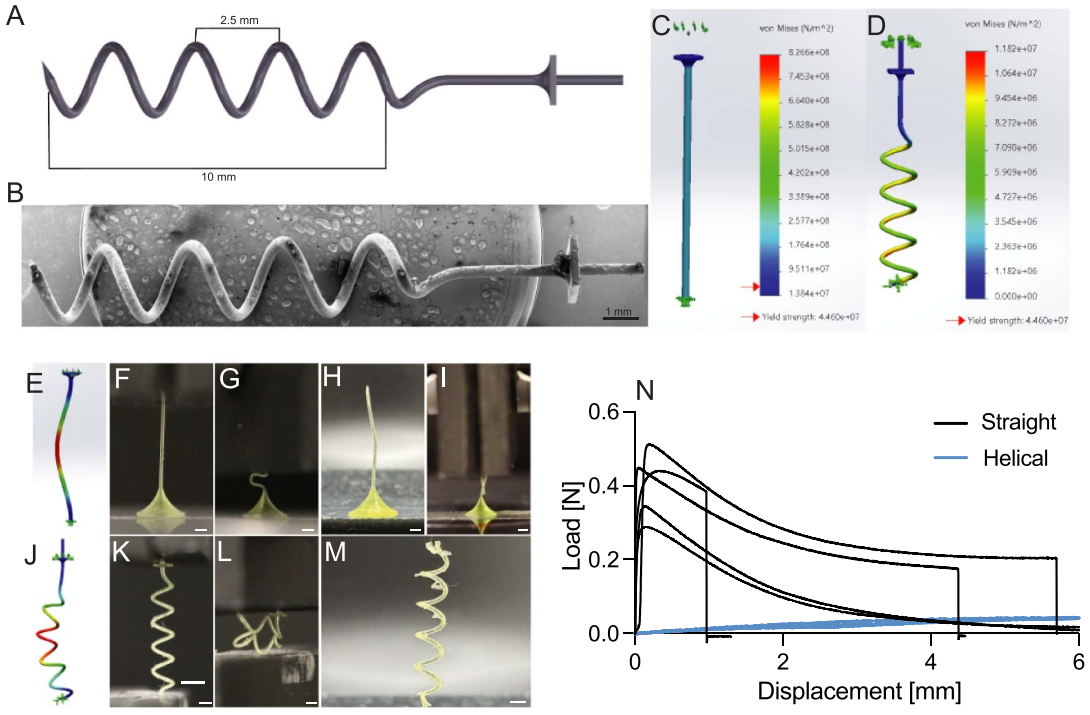

Figure 4. (A) Schematic of surgical helical catheter model (B) scanning electron micrograph of surgical helical catheter model (C) SolidWorks mechanical stress simulation of straight catheter (D) SolidWorks mechanical stress simulation of helical catheter (E) buckling simulation of straight catheter (F) straight catheter before buckling test (G) straight catheter during Instron mechanical testing (H) plastic deformation of straight catheter (I) fracture of straight catheter after buckling test (J) buckling simulation of helical catheter (K) helical catheter before Instron buckling test (L) helical catheter during Instron buckling test (M) helical catheter after buckling test (N) load-displacement curve of straight and helical catheters.

diameter at several points in time, we see that outflow at each outlet is equal, consistent with our CFD simulations (figures 3(D) and (E)). Droplet diameters corresponding to the four outlets increase in a similar linear trend, indicating equal volumetric flow rate throughout the straight catheter.

To further confirm the validity of the simulation and approximate *in vivo* conditions more closely, we investigated the diffusion of liquid through the outflow ports of a 4X scaled up catheter in a brain phantom model (Agarose 0.6% w/v) (figures 3(F)–(H)). The fabricated scaled up model had outlet diameters of 88.45, 132.8, 194.7 and 320.7 μm for outlets 1 through 4 respectively. Outlet sizes were measured through Scanning Electron Microscopy and their resulting flow rates were simulated on ANSYS by adjusting outlet size parameters to the fabricated sizes. A mixture of water and purple dye was pumped through the catheter at a flow rate of 0.67 μl min^{-1}, adjusted to maintain a consistent Reynolds number as before (0.0176) (table 1). We analyzed the resulting diffusion profile and calculated the relative magnitude of flow across outlets, finding similar distributions between experimental and computational results.

We next fabricated helical catheter prototypes along with a dedicated surgical insertion platform using additive manufacturing. We leveraged projection microstereolithography (PμSL), an additive manufacturing technology that provides 10 $\times$ 20 μm resolution. We used HTL20 resin with an initial layer exposure time of 5 s at laser intensity of 65.207 mW cm^{-2} and subsequent exposures of 1–3 s 39.67–48.9 mW cm^{-2}. Figure 4(A) shows the design of the helical model, featuring a helical component with a length of 10 mm, 4 revolutions and a pitch of 2.5 mm as well as a cylindrical portion with a length of 3 mm all with a thickness of 0.3 mm. The surgical prototype is also designed with a sharp, tapered tip to facilitate precise and minimally invasive entry into the brain during surgery and a rectangular base for stability when paired with the insertion apparatus (figure 4(B)).

We first characterized the mechanical behavior of SPIRAL, compared to traditional straight catheters. We posited that the helical structure would endow it with greater mechanical flexibility and minimize the likelihood of buckling on insertion. We used SolidWorks to simulate and compare the effect of mechanical stress on both helical and straight catheters after experiencing a prescribed displacement of 1 mm. Figures 4(C) and (D) compares the von mises stress distribution between the straight and helical catheters. The helical catheter experiences a maximum von mises stress of 10^7 Pa distributed over the entire helix, an order of magnitude less than its cylindrical counterpart, with a 10^8 Pa maximum von

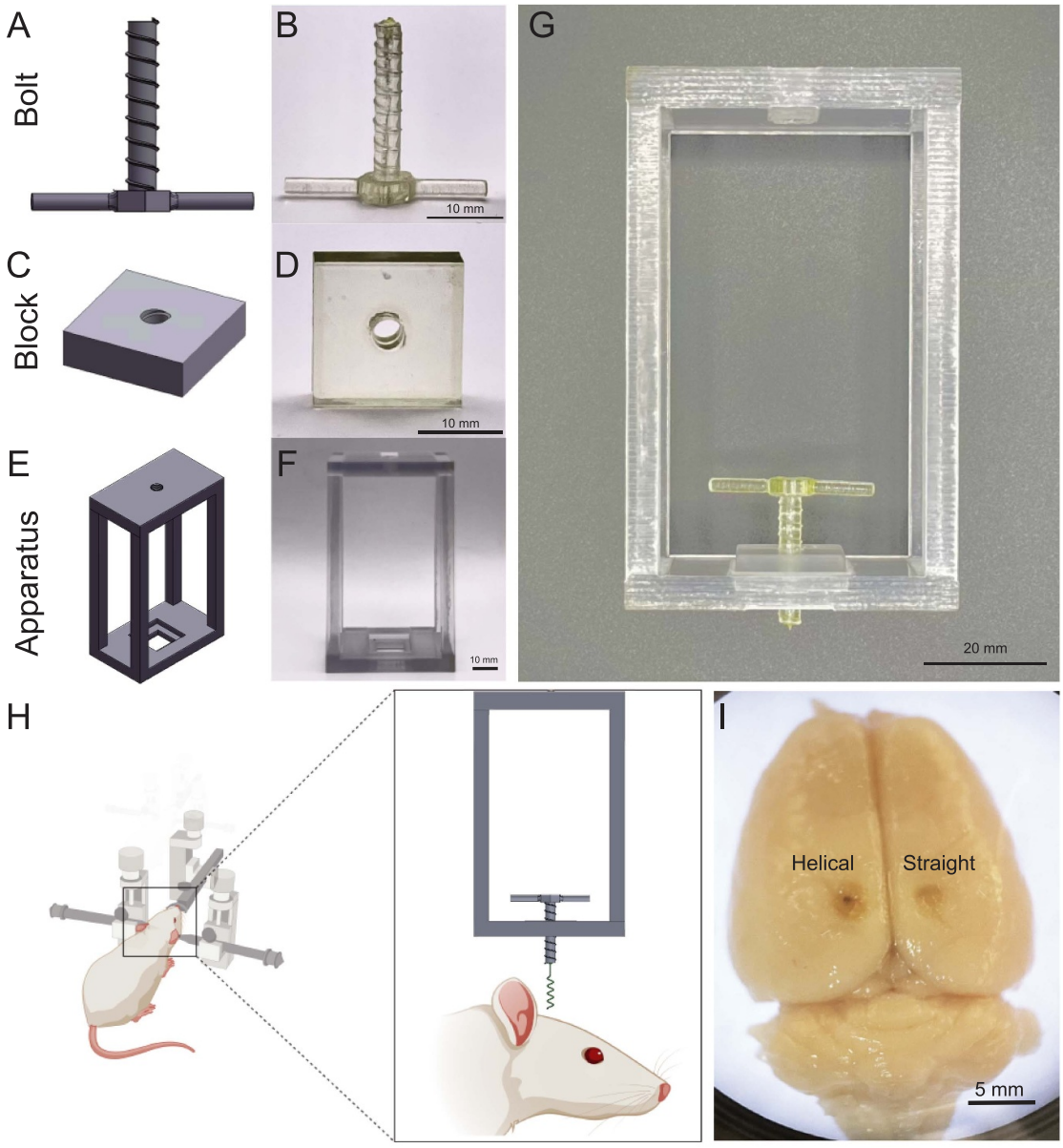

Figure 5. (A) SolidWorks schematic of surgical bolt (B) 3D printed bolt (C) SolidWorks schematic of surgical block (D) 3D printed block (E) schematic of surgical insertion apparatus (F) 3D printed surgical insertion apparatus (G) assembled block, bolt and surgical insertion apparatus (H) illustration of the surgical set up (I) straight implant vs helical implant in PFA 4% fixed rat brain, 5 weeks post-implantation.

mises stress concentrated at the tip. We validated this simulation by performing compression test trials at a rate of 5 mm min^{-1}. We observed that helical catheters were able to withstand a significantly higher displacement compared to the straight catheters, while remaining within the elastic deformation range (figures 4(E)–(M)). In addition, helical catheters that were subjected to more than 50% strain were able to return to their original form once the load was withdrawn (figure 4(M)). In contrast, straight catheters plastically deformed or fractured when subjected to the same strain (figures 4(H)–(I)). Figure 4(N) quantifies the buckling resistance of multiple trials done on the straight and the helical catheters. Cylindrical catheters were highly unstable during compression; in certain instances, they buckled and broke at higher displacements, while in others they deformed plastically and did not return to their original shape when the load was removed.

Unlike cylindrical straight catheters which can be inserted vertically into a brain, helical catheters must be rotated in to minimize vertical shear stress on tissue. To facilitate insertion of SPIRAL *in vivo*, we fabricated a customized insertion apparatus (figures 5(A)–(F)). The bolt in figures 5(A) and (B) is threaded with a pitch of 2.5 mm matching that of the helical surgical model and the block in 5 C–D. The cylindrical section of the bolt also has a cavity to insert the model in during the surgery (supplementary figures 2–5). The pitch matching of the insertion constructs ensures that the helical implant and insertion bolts turn at identical rates. We designed the

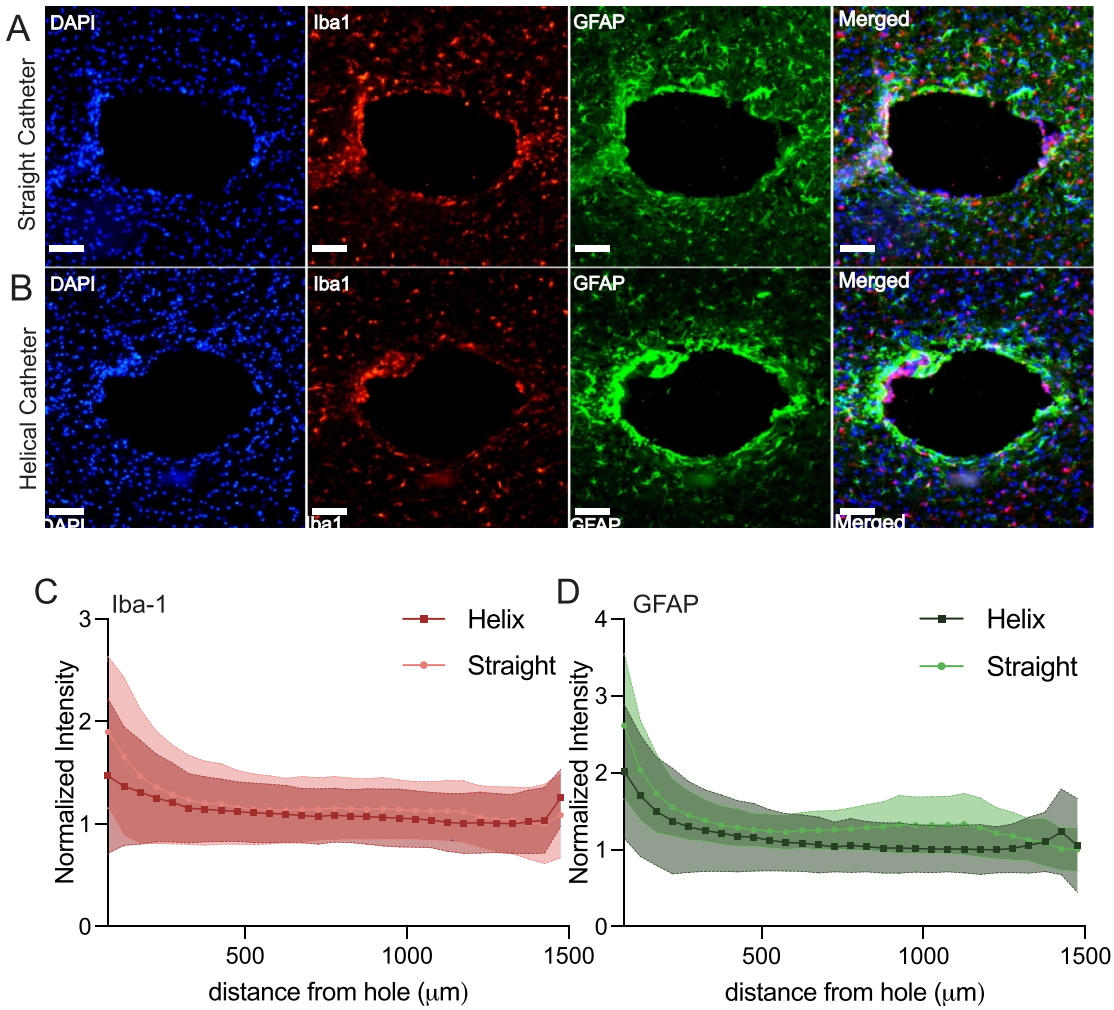

Figure 6. (A) Fluorescent microscopy images of DAPI, GFAP, Iba-1 and merged around the lesion of the straight (control) model 5 weeks post implantation (scale bar: 100 μm), (B) fluorescent microscopy images of DAPI, GFAP,Iba-1 and merged around the lesion of the helical model 5 weeks post implantation (scale bar: 100 μm) (C) intensity analysis profiles of Iba-1 (control and helical) (D) intensity analysis profiles of GFAP (control and helical).

apparatus in figures 5(E) and (F) with the four pillars to allow for easier access to the bolt during surgery while attached to a standard stereotactic apparatus (supplementary figure 4). Figure 5(G) shows the surgical insertion attachments assembled together.

We next conducted *in vivo* experiments to test our hypothesis that helical catheters induce no greater gliosis than straight catheters of similar size and materials. We co-implanted straight and helical catheters contralaterally in each animal. Figure 5(H) shows a schematic of the surgical set up with the use of the stereotax. We inserted the helical model under guidance from the assembled insertion apparatus, positioned above the animal's implant coordinates, while the bolt was slowly rotated into the brain tissue (figure 5(I)). To quantify gliosis induced by each implant, we stained transverse brain sections with markers for cell nuclei (DAPI), activated microglia (Iba1), and activated astrocytes (GFAP) (figures 6(A) and (B)). We analyzed the intensity of each stain as a function of distance from implant boundary. Both Iba1 and GFAP intensities peak around the implantation site and settle to within 10% of baseline at a distance of 526 and 626 μm, respectively, from implant border ($n = 4$). No statistically significant difference was observed between the control and helical model's peaks. This demonstrates that helical catheters induce gliosis at levels comparable to that induced by equivalent straight catheters.

3. Discussion

Intracerebral drug delivery systems can circumvent the drug delivery challenges imposed by the blood-brain barrier. We present a novel approach to tailor intracerebral catheter geometries for dosing regions with variable shapes. SPIRAL is a minimally invasive microfluidic helical catheter with computationally-derived outflow port sizes for tailored delivery profiles. We exemplify this approach with four equally-spaced outlet pairs along the length of a twice-revolved helix.

We used CFD modeling to analyze the effects of outlet size on fluid flow. Fluid mechanics models indicate that, at the microscale, pressure-driven fluid tends to follow the path of least resistance, which results in non-uniform flow distribution through a cylinder with multiple outflow holes [16, 17]. With the variation of the straight catheter's outlets' diameters to allow for mass flow rates' convergence, results in figure 2 support Hagen–Poiseuille's Law applicable to laminar flow, which dictates that flow rate is inversely proportional to the fourth power of radius [16, 17]. By decreasing the diameters of upstream outlets, relative to last and largest outflow port, equal flow rates are attained in straight catheters. Flow rate distribution differs when translating this to a helical shape, due to the added components of radial and centrifugal forces [18]. These forces, caused by the helical geometry, influence the fluid flow by creating a non-uniform pressure distribution within the cavity of the model [17–19].

Previous work has been done computationally to predict mass flow rate and the boli distribution across brain parenchyma during catheter-based infusions [20, 21]. Computational-guided bolus control is especially relevant due to the irregular shapes of brain structures [22]. Our approach here can be adapted, for example, to intentionally secure non-uniform outflows across each outlet pair. Achieving equal fluid distribution through Cerebrospinal Fluid ventricular shunts has been previously explored using CFDs software [23], and similarly, we corroborate the use of CFD software for intracerebral drug delivery and infusion-based catheters. One concern with intracerebral infusion catheters is the possibility of occlusion. In general, this is more likely to be the case when ports are smaller, and is believed to be secondary to a glial reaction. Interestingly, previous work has suggested that features with sizes smaller than 90 μm appear to be more resistant to clogging, and induce less gliosis [22, 24, 25]. We leverage this to our advantage in selecting smaller pore sizes (40,47,60,100 μm). Further chronic studies using helical implants will yield insight into the dynamics of pore obstruction.

In our study we utilized flow rates associated with diffusion, rather than convection-based transport of infusate in brain tissue. The Peclét number, a dimensionless parameter, is used to compare diffusive and convective fluid transport in a system [26]. A higher Peclét number indicates a flow dominated by convection, while a lower value signifies diffusion-driven transport [21]. While CED prioritizes broader and faster distribution of infusate in brain parenchyma, it also suffers from challenges of backflow and tissue injury due to high infusion pressures [13, 26]. Alternatively, SPIRAL utilizes a geometrical rationale to offer a complementary solution to the restricted bolus distribution radius of straight catheters.

The helical shape also offers distinct mechanical advantages over straight catheters. Previous reports have documented cases of intrathecal catheter fractures, leading to post-operative interventions [27]. While changing catheter material can mitigate this issue, mechanical properties such as flexibility and effective elasticity inherent to the geometry of a straight catheter can be substantially improved by utilizing a helical geometry [28, 29]. The topology of a helix distributes load more efficiently and reduces stress concentration points that may fail prematurely [28, 29]. This enhances buckling resistance and expands the range of elastic deformation for helical catheters (figure 4).

For all catheter designs, minimizing trauma experienced by brain tissue during insertion is crucial. This challenge is more observable when the implantable device is more mechanically elastic [14, 30]. Notwithstanding the helical catheter's mechanical robustness, its curvature presents a requirement for a distinct insertion method that minimizes trauma caused by its penetration. The insertion apparatus designed and assembled in figure 5 ensures stability of the catheter during the operation and steady rotation of the catheter as it is guided into the parenchyma of the brain, similar to a screw. This allowed the catheter's helical motion to be transformed linearly and results in a downward vertical motion, employing less mechanical force and stress on both the catheter and the brain tissue. Our *in vivo* results showing similar gliosis across catheter shapes support our hypothesis that the most prominent factor in the neuroinflammatory response to gliosis is the diameter. While the shape of the wound may differ in helical catheters, this may be explained by the angular path that the helical catheter takes during the insertion procedure, leading to a more elliptical imprint on the tissue (supplementary figure 7). However, the gliosis induced by straight and helical catheters as quantified by the activation of microglia and astrocytes is not significantly different (figures 6(C) and (D)). This may prompt more investigation into the mechanism of inflammatory induction caused by foreign bodies when introduced to brain tissue, particularly in the context of the implants' mechanical properties, as a diameter of 300 μm for two geometrically distinct objects, one more complex than the other, produced comparable gliosis in the tissue, consolidating that astrocytic and microglial activation is primarily directed by implant dimensions, and not overall structural shape.

Given the complex nature of neurological disorders, personalized therapy offers a promising approach for tailoring treatments based on the etiology and pathogenesis of each patient's condition [31]. For example, patients with neurological diseases such as epilepsy or Parkinson's may present the same symptoms, but may require different therapeutic approaches in line with the disease etiology [31–33]. Brain targets may also not be not congregated in one intracerebral region and instead dispersed

across the brain, where each regional dysfunction plays a role in the emergence of the disease.

For example, glioblastoma often metastasizes throughout the brain parenchyma by migrating along white matter tracts [34]. Previous research has been conducted to deliver drugs using catheter infusion devices. Of note, the Cleveland Multiport Catheter was used to treat glioblastoma with four independent microcatheters for drug infusion [35]. While the main rationale behind the multiple catheters used is to maximize drug penetrability in the target brain area, the use of multiple catheters for the infusion has the potential to produce complications during chronic implantation. This can be circumvented with a helical catheter as it minimizes the number of foreign objects occupying the brain parenchyma while permitting broad infusate distribution. Furthermore, the geometrical characteristics of a helix offer a broader range of opportunities for disease personalization mainly in the variation of the catheter's pitch, major diameter and hole distribution to be compatible with different disease conditions and parenchymal drug targets. In addition, the catheter's utility can be expanded into several other tissues as its structural features will prove beneficial in minimizing invasiveness while maximizing spatial distribution.

SPIRAL allows for more flexibility and personalization of catheter design. Some dimensions, however, may be limited by mechanical stresses as well as anatomic requirements. For example, the thickness of the skull imposes a minimum value on the helical pitch. If the pitch of the catheter is less than the thickness of the skull, a single downward rotation of the catheter may lead to the catheter tip coming into unintended contact with the skull. In our own studies we selected a pitch of 2.5 mm, larger than the rat skull thickness of 2.25 mm [36]. Increasing pitch decreases mechanical flexibility of the helix. While this could predispose catheters to fracture, it may also help ensure a straight insertion trajectory [37]. Decreased pitch could also increase the elliptical cross-section of the probe and lead to a greater insertion footprint (supplementary figure 7). Increasing helical diameter could broaden the volume of brain parenchyma targeted. However, this would complicate surgical planning as more brain structures may be affected along the insertion trajectory. Here the dimensions and rigid material we chose ensured adequate torque transmission during insertion. Torsional stiffness is inversely proportional to overall length and could be impeded with very long helices.

However, like other intracerebral catheters, it has several limitations, First, while computational simulations do not display any backflow, we were limited in experimentally validating the finding in the original scaled model due to the technical limits of the fabrication tools used. The Boston Micro Fabrication utilizes Projection μStereolithography technology, and offers a minimum hole diameter resolution of 40 μm, which limited our ability to manufacture the computational models at their original scale, but exhibited particularly remarkable feature accuracy for the surgical non-hollow model (figure 4(B)) [38]. Computational simulations also do not consider any change in effective pore diameter due to partial or complete occlusion over time after implantation. Moreover because of the curved structure of the helix spanning the Y axis it presents a need for navigation control of the device as it inhabits the cortical region upon implantation. Research shows that neuroinflammation can be dependent on the proximity of the foreign object to blood vessels, so it is crucial to take this into account during the design of the model for future therapeutic applications [39]. This work builds on previous efforts using computational methods to guide implant placement [22], and together could prove especially fruitful for helical devices to amplify drug target precision and minimize complications post-implantation.

4. Methods

4.1. CFDs model

For the CFDs simulations, we utilized Ansys Fluent within the Ansys Workbench environment. The helical model geometry was created in SolidWorks with the following specifications: a total height of 10 mm, 2 full revolutions, 1 pair of holes per half revolution (yielding 4 pairs of holes in total), a revolution diameter of 2 mm, and a pitch of 5 mm. For the straight catheter, the length was 16 mm, matching the approximate path length of the helical design, and 4 pairs of holes were placed at equal intervals from the inlet to the distal end. Both models were closed at the distal end. The designs were then exported as an .stl file and imported into Ansys Workbench. Upon import, the outlets were numbered pre-meshing (1 through 4), with outlet 1 being closest to an inlet and outlet 4 the furthest. The outlet diameters were then designated as driving parameter dimensions. The fluid and solid domains were defined, and a mesh with an element size of 5.36×10^{-4} m was generated. Water was selected as the working fluid, and the outlet surfaces were defined as output parameters. The solution was initialized with 50 iterations, followed by 100 iterations for the calculation. Convergence was monitored by ensuring that the scaled residuals for velocities in the x, y, and z directions, as well as continuity, dropped below 1×10^{-6}. Additionally, the mass flow rate at the outlets was tracked to ensure stability and the absence of fluctuations.

For mass-flow optimization, a parametric study was conducted to achieve equal mass flow rates through four outlets. Initially, all outlets had equal diameter of 100 μm. Laminar flow was specified, with an inlet mass flow rate of 2.78 $\times$ 10–9 kg s^{-1} (equivalent to 10 μl hr^{-1}). The optimization began by observing the mass flow rate at Outlet 1 (the closest

to the inlet) when its diameter was set to 100 μm. Iterative adjustments were then made in 10 μm decrements until the flow rate was nearly one-fourth of the total. Afterward, finer adjustments in increments as small as 1 μm were applied to precisely reach the target flow fraction. Once outlet 1 was optimized, a similar iterative process was applied to the remaining outlets to achieve equal flow distribution across all four. Minor readjustments were performed as needed on previously adjusted outlets to compensate for small flow variations introduced during subsequent iterations. This process was initially conducted for the straight catheter configuration for comparison.

4.2. Experimental verification of the computational model

To experimentally validate the flow rate results obtained through the simulation, the model was scaled up by a factor of 25 and 3D printed through the J750 (STRATASYS) 3D printer. The printer material used was VeroClear, also obtained through STRATASYS. The original viscosity of the fluid used was appropriately adjusted along with the flow rate to maintain Reynold's number obtained from the simulation. The catheter's inlet was attached to a syringe pump through a 20 ml syringe. And a corn syrup mixture of the adjusted viscosity was pumped through the scaled-up model's inlet at a pressure of 5.52064 ml min^{-1}. Data was recorded using the fluid imaging system provided by the SITES lab at NYUAD, which consisted of two vertically angled mirrors to reflect an image for the DSLR camera (Nikon) to capture every 10 s, using the GraphPad PRISM software.

For further validation of the simulation, an agarose diffusion study was conducted on a brain phantom model using freshly prepared and casted 0.6% agarose in PBS. A 4X straight catheter model was fabricated using the microArch S240 3D printer with 10 μm *XY* resolution and 20 μm layer thickness. To achieve optimum model outlet resolution, the first image was projected onto the platform and exposed for a duration of 4.5 s with a laser intensity of 45 mW cm^{-2}. Lower intensities and durations within the range of 30–45 mW cm^{-2} for durations of 1 and 3 s were utilized when subsequent projected images consisted of the catheter outlets while higher laser values were applied for curing of model supports and base. The printed model was deplatformed, flushed and submerged in Isopropanol overnight and allowed to dry before use in the experiment. The catheter was carefully inserted into a 0.6% agarose block with 1.5 cm height and the inlet fixed into the mold to avoid backflow. A mixture of water and dye was prepared and injected through the inlet at a flow rate of 0.67 μl min^{-1}. Data was recorded using the fluid imaging system provided by the SITES lab at NYUAD, which consisted of two vertically angled mirrors to reflect an image for a DSLR camera (Nikon) to capture at frame rate of 1 frame s^{-1}. Images of 3 trials were processed using a MACROS code on ImageJ and number of pixels of infused liquid was plotted and its slope calculated. The ratio of each outlet's contribution to the overall flow was then processed and compared to the simulation's outlet flow rate contribution using the GraphPad Prism software. We compared these results to that obtained from a ANSYS simulation. To minimize errors due to printing resolution, we measured the actual outlet size in the print and used these for the comparative simulation model.

4.3. Model design, fabrication and characterization

The implantable straight and helical catheter models were designed on SolidWorks 2023 software. Large area micro-stereolithography 3D fabrication of the models was done using the microArch S240 3D Printer (Boston Micro Fabrication) with 10 μm *XY* resolution and 20 μm layer thickness. The material that was used for the printing was the HTL resin provided by Boston Micro Fabrication. The first image was projected onto the platform and exposed for a duration of **5 s** with a laser intensity of 65.207 mW cm^{-2}. Subsequent images were exposed to laser intensities within the range of 39.67 and 48.9 mW cm^{-2} for exposure durations of 1 and 3 s. The printed models were then removed from the platform and rinsed with isopropyl alcohol and allowed to dry. Simulations were performed on SolidWorks to evaluate the mechanical performance of the catheters. The ends of each catheter were fixed for the simulation. A prescribed displacement of 1 mm was then applied to both the straight and helical catheter. For each catheter, the von Mises stress distribution was analyzed, and failure was determined based on the material's yield criterion. To experimentally validate the mechanical simulation, we performed a compression test to both the straight and helical catheters using a universal testing system (Instron 5960 series). We used a grip attachment to fix both ends of the specimen and prescribed a displacement rate of 5 mm per minute. The test was terminated upon specimen failure or when the total displacement reached the machine's safety limit.

4.4. *In vivo* studies

To minimize tissue injury during the insertion of the helical model, a screw, a bolt, and an attachment for the stereotactic device were designed using SolidWorks 2023 software. All parts were 3D printed on J750 (STRATASYS) with VeroClear material. The screw and bolt block were right threaded with a pitch matching that of the helical device (2.5 mm). The screw had a hole of 0.35 mm for the straight distal portion of the implant to be inserted epoxied into, for stability. The attachment includes a cavity that allows the bolt block to be placed during the surgical procedure. We used Sprague Dawley rats to compares gliosis and scarring in response to straight and helical implants.

Sprague Dawley Rats were prepared for the surgery and anesthetized with Isoflurane. Their crown was shaved and disinfected with alternating betadine and ethanol scrubs. Animals were then placed on the stereotaxic device. Animals had two contralateral burr holes drilled at coordinates (−5.00 mm AP, −2.21/2.21 mm ML relative to bregma). Each animal had a straight catheter inserted on one side, and a helical catheter contralaterally. The helical device was assembled with the surgical bolt by inserting its straight end to the hole of the bolt and epoxied. The bolt, with the helical implant now attached, were then placed in the bolt block and slowly rotated clockwise at the point of entry of the burr hole. Once the distal helical section as fully inserted and the proximal straight end was the only visible portion, it was then cut using sharpened surgical scissors, to separate the insertion apparatus from the implant. Following the full implantation of the device, the animals' health was monitored for 5 weeks and they were then prepared for perfusion. Anesthetized animals were subject to cardiac perfusion using Phosphate Buffer Solution, and then perfused using 4% freshly prepared Paraformaldehyde. The brains of the animals were then extracted and submerged in 4% PFA for 24 h and were then placed in 30% sucrose solution until the brain was observed to have sunk.

4.5. Immunohistochemistry

Brains were embedded with cryo-embedding medium (Tissue-Tek) and left in −80 °C to freeze as preparation for cryosectioning. 30 μm thin sections were obtained with the Cryostat (Leica CM1950) at a temperature of −18 °C, and placed on SuperFrost Gold microscope slides. To determine the neuroinflammatory response of the implants in the brains, microglia and astrocyte cells were stained. The brain sections were rinsed with 1X PBS and treated with a blocking buffer (10% Normal Donkey Serum in 0.5% Triton-X) for an hour. Following the blocking step, the brain sections were incubated overnight in iba-1 and GFAP primary antibodies in 10% NDS/0.5% Triton-X at a ratio of 1:200 for both. After rinsing the primary antibodies with 1X PBS, the Iba-1 and GFAP antibody were tagged with the secondary antibodies Alexa Fluor 594 donkey anti-goat and Alexa Fluor 88 donkey anti-mouse respectively and were left to incubate for 2 h, followed by a 1X PBS rinse and a DAPI (1:1000) 20 min incubation and mounted in gold fluorescent medium. The sections were imaged using an Eclipse ti2-E Widefield Fluorescence Microscope (Nikon Instruments Inc.) and all images for each antibody were captured at the same exposure and intensity settings to allow for further intensity analysis. GFAP and iba-1 Intensity profiles of multiple brain sections at the regions of the implantation were generated using Circ_M MATLAB program (Capadona Lab, Case Western Reserve University) and the data plotted and normalized using the GraphPad PRISM 10.0 software.

Data availability statement

All data that support the findings of this study are included within the article (and any supplementary files).

Acknowledgment

This work was supported by the Center for Translational Medical Devices and Center for Brain Health at NYU Abu Dhabi. We acknowledge NYU Abu Dhabi Core Technology Platforms for equipment and Dr Oraib Al-Ketan's technical assistance, the Center for Stability, Instability, and Turbulence (SITE) Lab at NYU Abu Dhabi for droplet-measuring imaging, and the Capadona Lab at Case Western Reserve university for the MATLAB script to analyze immunofluorescence images.

Ethics statement

All animal experiments were performed in accordance with protocols approved by the Institutional Animal Care and Use Committee at New York University Abu Dhabi (Protocol 21-0007).

Author contributions

Abdel-Hameed Dabbour 0000-0002-6762-2563
Investigation (supporting), Methodology (supporting), Writing – review & editing (supporting)

Heba T Naser
Investigation (supporting), Project administration (supporting), Writing – review & editing (supporting)

References

[1] Feigin V L, Vos T, Nichols E, Owolabi M O, Carroll W M, Dichgans M, Deuschl G, Parmar P, Brainin M and Murray C 2020 The global burden of neurological disorders: translating evidence into policy *Lancet Neurol.* **19** 255–65
[2] Bhunia S, Kolishetti N, Vashist A, Yndart Arias A, Brooks D and Nair M 2023 Drug delivery to the brain: recent advances and unmet challenges *Pharmaceutics* **15** 2658
[3] Ayub A and Wettig S 2022 An overview of nanotechnologies for drug delivery to the brain *Pharmaceutics* **14** 224
[4] Roberts R L, Fine R E and Sandra A 1993 Receptor-mediated endocytosis of transferrin at the blood-brain barrier *J. Cell Sci.* **104** 521–32
[5] Teleanu D M, Chircov C, Grumezescu A M, Volceanov A and Teleanu R I 2018 impact of nanoparticles on brain health: an up to date overview *J. Clin. Med.* **7** 490
[6] Lesniak M S and Brem H 2004 Targeted therapy for brain tumours *Nat. Rev. Drug Discov.* **3** 499–508
[7] D'Amico R S, Aghi M K, Vogelbaum M A and Bruce J N 2021 Convection-enhanced drug delivery for glioblastoma: a review *J. Neurooncol.* **151** 415–27

[8] Hollingworth M and Zacharoulis S 2022 Infusion-related side-effects during convection enhanced delivery for brainstem-diffuse midline glioma/diffuse intrinsic pontine glioma *J. Neurooncol.* **159** 417–24
[9] Raghavan R, Brady M L, Rodríguez-Ponce M I, Hartlep A, Pedain C and Sampson J H 2006 Convection-enhanced delivery of therapeutics for brain disease, and its optimization *Neurosurg. Foc.* **20** E12
[10] Krauze M T, Saito R, Noble C, Tamas M, Bringas J, Park J W, Berger M S and Bankiewicz K 2005 Reflux-free cannula for convection-enhanced high-speed delivery of therapeutic agents *J. Neurosurg.* **103** 923–9
[11] Lueshen E, Tangen K, Mehta A I and Linninger A 2017 Backflow-free catheters for efficient and safe convection-enhanced delivery of therapeutics *Med. Eng. Phys.* **45** 15–24
[12] Schomberg D, Wang A, Wang A, Marshall H, Sillay K, Miranpuri G and Miranpuri G 2013 Ramped-rate vs continuous-rate infusions: an *in vitro* comparison of convection enhanced delivery protocols *Ann. Neurosci.* **20** 59–64
[13] Guarnieri M, Carson B S and Jallo G I 2008 Catheters for chronic administration of drugs into brain tissue *Drug Delivery Systems* ed K K Jain (Humana Press) pp 109–17
[14] Spencer K C, Sy J C, Ramadi K B, Graybiel A M, Langer R and Cima M J 2017 Characterization of mechanically matched hydrogel coatings to improve the biocompatibility of neural implants *Sci. Rep.* **7** 1952
[15] DeVos S L and Miller T M 2013 Direct intraventricular delivery of drugs to the rodent central nervous system *J. Vis. Exp.* **12** e50326
[16] Stokes G G 1880 On the theories of the internal friction of fluids in motion, and of the equilibrium and motion of elastic solids *Mathematical and Physical Papers* vol 1 (Cambridge University Press) pp 75–129
[17] Kirby B J 2010 *Micro- and Nanoscale Fluid Mechanics: Transport in Microfluidic Devices* (Cambridge University Press)
[18] Totorean A F, Bernad S I and Susan-Resiga R F 2016 Fluid dynamics in helical geometries with applications for by-pass grafts *Appl. Math. Comput.* **272** 604–13
[19] Manlapaz R L and Churchill S W 1980 Fully developed laminar flow in a helically coiled tube of finite pitch *Chem. Eng. Commun.* **7** 57–78
[20] Raghavan R and Brady M 2011 Predictive models for pressure-driven fluid infusions into brain parenchyma *Phys. Med. Biol.* **56** 6179–204
[21] Rosenbluth K H, Eschermann J F, Mittermeyer G, Thomson R, Mittermeyer S and Bankiewicz K S 2012 Analysis of a simulation algorithm for direct brain drug delivery *NeuroImage* **59** 2423–9
[22] Ramadi K B, Bashyam A, Frangieh C J, Rousseau E B, Cotler M J, Langer R, Graybiel A M and Cima M J 2020 Computationally guided intracerebral drug delivery via chronically implanted microdevices *Cell Rep.* **31** 107734
[23] Weisenberg S H, TerMaath S C, Barbier C N, Hill J C and Killeffer J A 2018 A computational fluid dynamics simulation framework for ventricular catheter design optimization *J. Neurosurg.* **129** 1067–77
[24] Dagdeviren C *et al* 2018 Miniaturized neural system for chronic, local intracerebral drug delivery *Sci. Transl. Med.* **10** eaan2742
[25] Ramadi K B, Dagdeviren C, Spencer K C, Joe P, Cotler M, Rousseau E, Nunez-Lopez C, Graybiel A M, Langer R and Cima M J 2018 Focal, remote-controlled, chronic chemical modulation of brain microstructures *Proc. Natl Acad. Sci.* **115** 7254–9
[26] Stine C A and Munson J M 2019 Convection-enhanced delivery: connection to and impact of interstitial fluid flow *Front. Oncol.* **9** 966
[27] Kinch L and Kohan L 2020 Headaches of catheters past: a case report of persistent cerebrospinal fluid accumulation from a prior nonfunctioning intrathecal drug delivery catheter *Neuromodulation* **23** 1052–3
[28] Liljenhjerte J, Vudayagiri S, Solms N V and Nygaard J V 2021 Stability of periodically supported slender structures and quantification of helix formation *Appl. Eng. Sci.* **8** 100070
[29] Timoshenko S P and Gere J M 2012 *Theory of Elastic Stability* (Courier Corporation)
[30] Jorfi M, Skousen J L, Weder C and Capadona J R 2015 Progress towards biocompatible intracortical microelectrodes for neural interfacing applications *J. Neural Eng.* **12** 011001
[31] Arora R and Baldi A 2024 Revolutionizing neurological disorder treatment: integrating innovations in pharmaceutical interventions and advanced therapeutic technologies *Curr. Pharm. Des.* **30** 1459–71
[32] Krajcovicova L, Klobusiakova P and Rektorova I 2019 Gray matter changes in Parkinson's and Alzheimer's disease and relation to cognition *Curr. Neurol. Neurosci. Rep.* **19** 85
[33] Shariff S, Kantawala B, Xochitun Gopar Franco W, Dejene Ayele N, Munyangaju I, Esam Alzain F, Nazir A, Wojtara M and Uwishema O 2024 Tailoring epilepsy treatment: personalized micro-physiological systems illuminate individual drug responses *Ann. Med. Surg. Lond.* **86** 3557–67
[34] Seker-Polat F, Pinarbasi Degirmenci N, Solaroglu I and Bagci-Onder T 2022 Tumor cell infiltration into the brain in glioblastoma: from mechanisms to clinical perspectives *Cancers* **14** 443
[35] Vogelbaum M A *et al* 2019 First-in-human evaluation of the Cleveland Multiport Catheter for convection-enhanced delivery of topotecan in recurrent high-grade glioma: results of pilot trial 1 *J. Neurosurg.* **130** 476–85
[36] Zhou R, Li Y, Cavanaugh J and Zhang L 2020 Investigate the variations of the head and brain response in a rodent head impact acceleration model by finite element modeling *Front. Bioeng. Biotechnol.* **8** 172
[37] Dym C L 2009 Consistent derivations of spring rates for helical springs *J. Mech. Des.* **131** 071004
[38] Galloway L 2021 Demystifying 3D printing resolution, accuracy, and precision (Blog Post) (available at: https://bmf3d.com/blog/demystifying-3d-printing-resolution-accuracy-and-precision/)
[39] Kozai T D Y, Jaquins-Gerstl A S, Vazquez A L, Michael A C and Cui X T 2015 Brain tissue responses to neural implants impact signal sensitivity and intervention strategies *ACS Chem. Neurosci.* **6** 48–67